

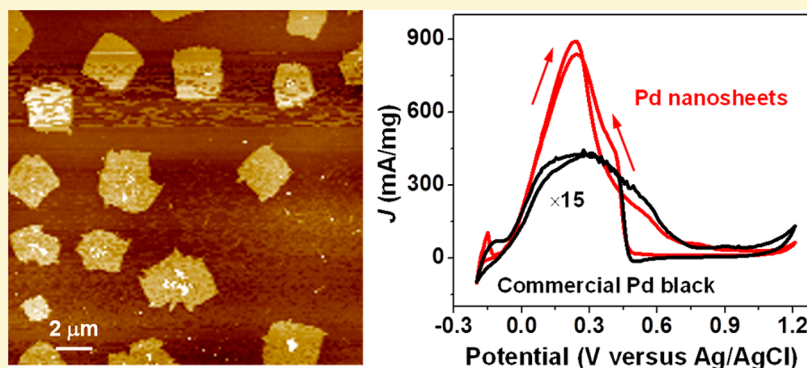
Ionic Layer Epitaxy of Nanometer-Thick Palladium Nanosheets with Enhanced Electrocatalytic Properties

Xin Yin,[†] Qinyi Chen,[†] Peng Tian,^{†,‡} Pei Zhang,[†] Ziyi Zhang,[†] Paul M. Voyles,[†] and Xudong Wang^{*,†}

[†]Department of Materials Science and Engineering, University of Wisconsin—Madison, Madison, Wisconsin 53706, United States

[‡]Department of Chemical Engineering, Dalian University of Technology, Dalian 116023, China

S Supporting Information



ABSTRACT: Large surface area-to-volume ratio with plenty of accessible electrochemically active sites presents metal nanosheets a highly efficient catalyst material. However, a facile and effective synthesis of metal nanosheets with nanoscale thicknesses, macroscopic sizes, and desired crystal facets is still a grand challenge. Here, we report the synthesis of free-standing Pd nanosheets by ionic layer epitaxy (ILE), which employs a cationic oleylamine monolayer at the water–air interface as a soft template to guide the nanosheet growth. The Pd nanosheets exhibited a quasi-square morphology with a uniform thickness of ~ 2 nm and sizes ranging from 1 to 6 μm . Owing to the extremely large surface-to-volume ratio and the exposure of mixed surface crystal facets, the Pd nanosheets exhibited high activity in formic acid oxidation compared to the commercial Pd black and other reported Pd nanostructures. This work presents a simple and effective way to prepare metal nanosheets with nanometer-scale thickness control.

Metal nanocrystals have attracted tremendous interests due to their promising applications in catalysis, plasmonics, and magnetism.^{1–7} Among them, palladium (Pd) is a multifunctional metallic material that has shown great potentials in electrocatalysis for fuel cell reactions,^{8–11} catalysis for organic cross-coupling reactions,^{12–14} and hydrogen sensing.^{15–17} Toward improving the catalytic performance, considerable efforts have been focused on shape-controlled synthesis of Pd nanocrystals. Pd nanocubes enclosed by the (100) facets offered a superior catalytic activity in formic acid oxidation compared to Pd octahedrons enclosed by the (111) facets.¹⁰ The quasi-2D morphology of Pd was recently demonstrated as an even more efficient catalyst owing to the high surface area/volume ratio with a myriad of active sites exposed and rapid charge transport across the ultrasmall thickness. For example, 2.3 nm Pd nanosheets showed a much higher catalytic activity than Pd tetrahedrons and commercial Pd black for various alcohol/formic acid oxidation reactions.⁹ These small Pd nanosheets were dominated by the most stable (111) facet, which however is not the most catalytically active surface. Synthesis of Pd nanosheets with the more active (100)

facets might further improve the catalytic performance. Nevertheless, due to the nonlayered face-centered cubic (fcc) crystal structure of Pd, it is still fairly challenging to synthesize Pd nanosheets with well controlled size, thickness, and crystal facets, which are critical to rational design of catalytic activities. Prevailing method of synthesizing Pd nanosheets was relying on selective absorption of surfactants to restrict the out-of-plane growth.^{8,18,19} However, due to the limited sizes of surfactant micelles assembled in bulk solution, these strategies often yielded very small particle sizes (< 50 nm) and were incapable of controlling the sheet thickness down to the nanometer regime.

Ionic layer epitaxy (ILE), a recently developed solution-based synthesis technique, has been successful in growing nanometer thick two-dimensional (2D) ZnO nanosheets with sizes up to tens of micrometers.^{20–22} In ILE, a self-assembled amphiphilic monolayer at the water–air interface was used as a

Received: February 6, 2018

Revised: April 29, 2018

Published: April 30, 2018

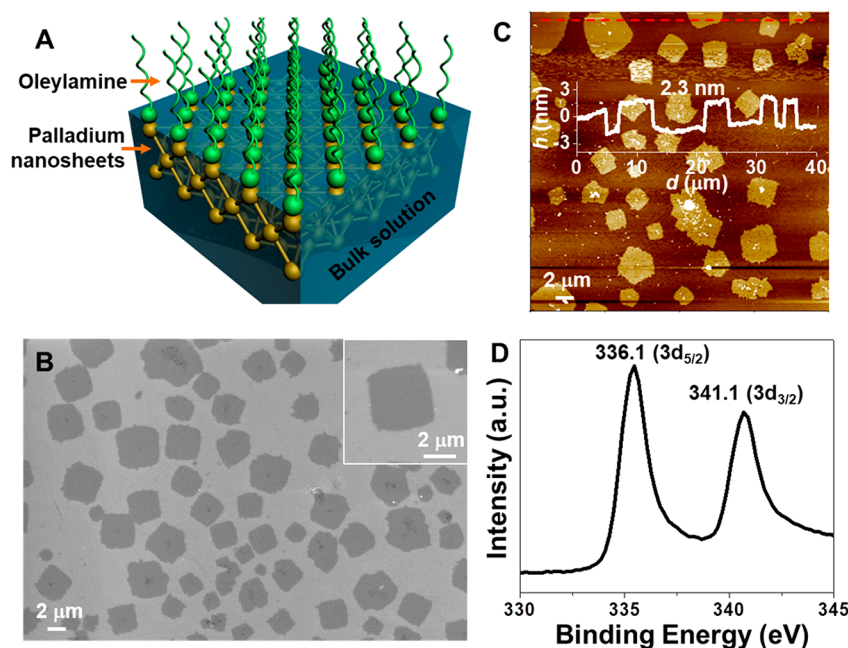


Figure 1. Synthesis of Pd nanosheets. (A) Schematic of ILE growth for Pd nanosheets. Oleylamine amphiphilic monolayer is represented by an array of green balls as the headgroups and a helical tail on each ball as the carbon chain. Pd atoms are represented by yellow balls. (B) Large scale SEM image showing quasi-square Pd nanosheets on Si substrate. (C) AFM topography image showing the nanometer thickness and excellent surface flatness of the nanosheets. Inset is the height profile along the red dashed line revealing the thickness is 2.35 nm. (D) XPS spectrum of characteristic X-ray peak of Pd $3d_{5/2}$ and $3d_{3/2}$.

soft template to guide the nucleation and growth of 2D nanosheets underneath. The packing density of amphiphilic molecules in the monolayer controls the thickness of the nanosheet with a resolution down to one unit cell. It is hypothesized that if an appropriate pair of amphiphilic molecule and aqueous synthesis protocol is identified, it will be possible to grow 2D metal nanosheets by ILE with control thickness and large sizes. In this work, we demonstrated a successful ILE growth of ultrathin Pd nanosheets using an oleylamine monolayer at the water–air interface. The Pd nanosheets exhibited a quasi-square shape and a tunable thickness from 2.0 to 3.2 nm. Owing to the ultrasmall thickness, high crystallinity, and exposure of active crystal facets, the Pd nanosheets demonstrated a more than 30 times higher catalytic activity compared to the commercial Pd black. This work offered a promising approach toward rational design and synthesis of ultrathin metallic 2D nanosheets with enhanced functionality.

RESULTS AND DISCUSSION

The schematic ILE synthesis of Pd nanosheets is shown in Figure 1A (synthesis details are included in the Experimental Section). In the growth process, the ionized oleylamine molecules self-assembled into a positively charged monolayer at the water–air interface. Negatively charged anionic groups (e.g., PdCl_4^{2-}) were attracted to the interface, forming an ultrathin precursor-concentrated region beneath the monolayer. At an elevated temperature of 60 °C and in the presence of a reducing agent (HCHO), Pd crystals were nucleated and grown within the confined region forming 2D nanosheets. The as-synthesized Pd were transferred onto a Si wafer surface by simply dipping the substrate into the solution and then lifting. As shown in Figure 1B, the nanosheets covered ~51.2% of the surface area without any overlapping, showing a high yield of

single-layered growth. All the nanosheets appeared to be quasi-squares with side lengths ranging from 2 to 4 μm . An enlarged image of a single nanosheet revealed the edges were not completely straight with spikes extended out particularly at the corner regions (inset of Figure 1B and Figure S1). Atomic force microscopy (AFM) was used to characterize the surface flatness and thickness (Figure 1C). All the nanosheets exhibited a uniform thickness of 2.4 nm, as confirmed by the height profile scan across several nanosheets (inset of Figure 1C). The surface of nanosheets was generally very flat with a roughness factor of $R_a = 0.18$ nm. However, a few small nanoparticles were also found at the center of some nanosheets. They were believed to be excessive nucleates formed during extended nanosheet growth time.²¹ Further extending the reaction time led the formation of a secondary layer at the center of the first layer, accompanied by a larger overall lateral size (~4–5 μm , Figure S2). The height of the secondary layer was 2.0 nm, slightly larger than the first layer (1.7 nm). This morphology presents a good indication of the layer-by-layer growth mode of the nanosheet structure by ILE.

X-ray photoelectron spectroscopy (XPS) was implemented to study the elemental characteristics of the nanosheets. A full wavelength survey scan of the nanosheets annealed to oleylamine revealed multiple strong elemental signals from Si 2p at 104.08 eV, C 1s at 285.08 eV, N 1s at 400.08 eV, O 1s at 533.08 eV, and Pd 3d at 336.08 and 341.08 eV (Figure S3). The signals of Si and O were believed from the SiO_2 -coated Si substrates, and the C and N signals were residues from the oleylamine monolayer being transferred together with the nanosheets. From the individual scan of Pd, the peaks of Pd $3d_{5/2}$ at 336.1 eV and $3d_{3/2}$ at 341.1 eV matched well with the characteristic binding energies of metallic Pd, suggesting the formation of metallic Pd nanosheets.

The crystal structure of Pd nanosheets was characterized by transmission electron microscopy (TEM). The ultrathin

nanosheets remained its original shape after being transferred to the holey carbon TEM grid (Figure S4). Selective area electron diffraction (SAED) pattern collected from the nanosheet region showed a clear polycrystalline feature (inset of Figure 2A). The concentric diffraction rings could be

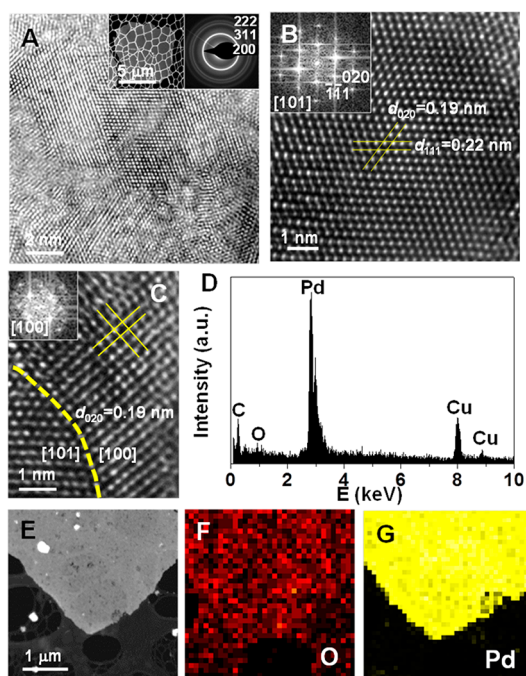


Figure 2. Crystal structure and composition characterization of the nanosheets. (A) HRTEM image showing the crystalline domains with different crystallographic orientation. Inset is the corresponding selective area electron diffraction pattern. (B) HRTEM image on one crystalline domain showing a perfect (101) crystal facet without any observable defects. Inset is fast Fourier transform pattern (FFT). (C) HRTEM image showing two crystalline domains with the exposed (101) and (100) facets. A grain boundary is indicated by a yellow dashed line. Inset is FFT of the (100) facet. (D) EDX spectrum. (E) Low-magnification TEM image and corresponding EDX elemental mapping of (F) O and (G) Pd.

indexed to {200}, {311}, and {222}, matching well to the JCPDS card (No. 46-1043), further confirming the metallic fcc Pd structure. High-resolution TEM (HRTEM) image revealed the nanosheet was composed of crystalline domains with a size of 10–15 nm (Figure 2A). These domains exhibited different orientation but all had the same thickness. This growth phenomenon further confirmed the ILE mechanism that nanosheet nucleation and growth is confined within the nanometer thick precursor-concentrated region underneath the amphiphilic monolayer, regardless of the crystal orientation. Based on the oriented attachment principle,²² the polycrystalline feature was likely because the bonding force between Pd atoms was not high enough to overcome the environmental resistance for domain rotation, particularly the strong steric hindrance from the carbon tails of oleylamine in the monolayer. HRTEM of a single domain revealed a clear and sharp lattice of the Pd crystal, and no indication of amorphous or disordered region could be observed (Figure 2B). The corresponding fast Fourier transform (FFT) pattern confirmed the crystalline domain had an exposed (101) surface plane, which has also been seen from Pd nanosheets synthesized by other approaches.²³ The lattice spacing of the (020) and (111)

planes were measured to be 0.19 and 0.22 nm, respectively. The high-energy (100) facet was also observed coexisting with the (101) facet (Figure 2C). The orientation was confirmed by FFT (inset of Figure 2C). Exposure of the highly active (001) facets was favorable for the Pd nanosheets to show enhanced catalytic performance.^{10,24} The energy-dispersive X-ray spectrum (EDX) taken from the nanosheet showed a strong Pd signal (Figure 2D), while only negligible O signal was detected. EDX elemental mapping showed that the Pd signal clearly outlined the shape of nanosheet (Figure 2F), whereas the O signal was uniformly distributed over the entire carbon supported area (Figure 2G). The structural and elemental characterizations confirmed that the nanosheets were pure metallic Pd phase with no oxidation features involved.

Our previous study has revealed that the packing density of ionized amphiphilic monolayer had strong influences on the width of precursor-concentrated region and thus could fine-tune the nanosheet thickness.²² To test this principle in the Pd nanosheet growth system, four packing densities were used by spreading 10, 14, 16, and 18 μL of oleylamine solution onto a 4.72 cm^2 reactor surface. The corresponding packing densities were estimated to be 3.61×10^{-5} , 5.04×10^{-5} , 5.77×10^{-5} , and 6.49×10^{-5} mol/m^2 , respectively. Figures 3A–D are large scale SEM images of as-synthesized Pd nanosheets transferred on Si substrates. All of packing densities yielded Pd nanosheets with similar quasi-square geometry. The nanosheet densities were nearly unchanged, but the size of nanosheets obviously increased as the packing density increased. Many fiber-like structures were observed from the lowest packing density system (Figure 3A), possibly due to the insufficient precursor quantity for the formation of continuous nanosheets. The AFM topography images (Figures 3E–H) and corresponding height profiles (Figures 3I–L) further revealed the morphology change as a function of the surfactant packing density. All the nanosheets exhibited an equivalently good surface flatness ($R_a = 0.20$ nm) and uniform thickness, evidencing the high-reproducibility of ILE in synthesizing 2D nanosheet. As the packing density increased, the nanosheet thickness raised monotonically from 2.0 nm to 2.3, 2.4, and 3.2 nm. Further statistical analysis of over 20 nanosheet samples revealed a correlation between the nanosheets' thickness and size and the surfactant packing density, consistent with those observed from the growth results of ZnO nanosheets²² (Figures 3M and 3N). The thickness of Pd nanosheets increased from 2.3 ± 0.2 to 3.1 ± 0.2 nm as a functional of the packing density. Meanwhile, the side length increased accordingly from 1.83 ± 0.36 μm to 2.20 ± 0.35 , 3.11 ± 0.62 , and 5.24 ± 1.14 μm . This size and thickness increase following the packing density of surfactant monolayer was an immediate result of the enriched precursor ion concentration in the nanosheet nucleation region, which is a primary ILE growth kinetics.

Pd has been considered as an efficient anodic, monometallic electrocatalyst for formic acid oxidation (FAO) in a direct formic acid fuel cell.^{25,26} Nanostructured morphology is always favorable for catalytic applications due to the high surface area/volume ratio and abundant active surface active sites. In addition, the exposure of highly active (100) facets might further improve the nanosheet's catalytic performance. In order to investigate the catalytic properties associated with the unique geometry and structural feature, Pd nanosheets with an average thickness of 2.6 nm were tested for FAO and compared to a commercial Pd black sample (Thermo Fisher, Pd powder with average size of ~ 40 nm, Figure S5). Figure 4A shows the mass

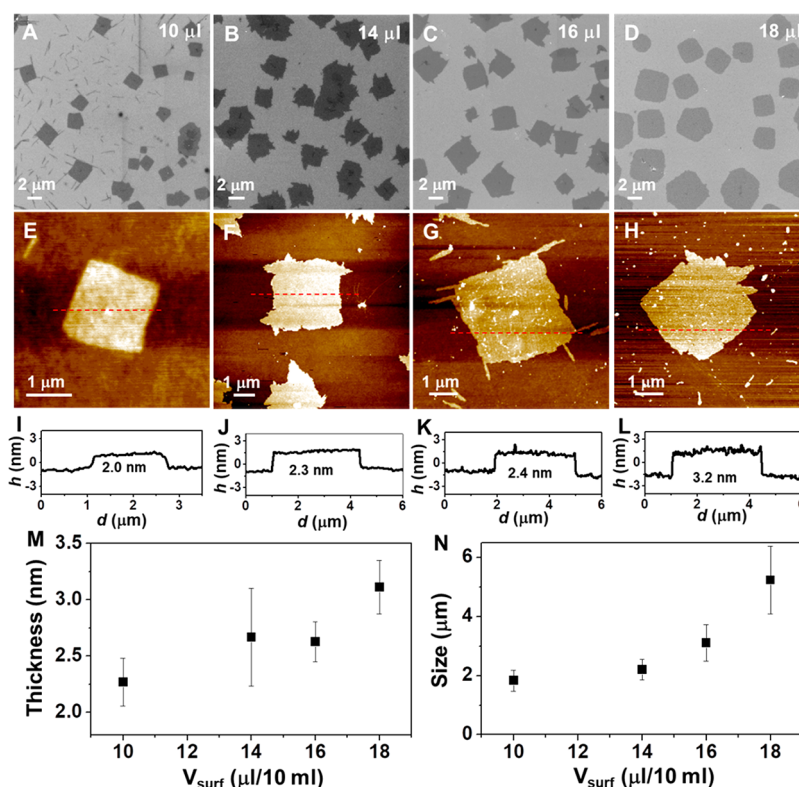


Figure 3. Influence of the oleylamine monolayer packing density on the size and thickness of Pd nanosheets. (A–D) SEM images, (E–H) AFM topography images, and (I–L) height profiles along the red dashed lines in corresponding AFM topography images of Pd nanosheets grown with (A, E, I) 10 μL , (B, F, J) 14 μL , (C, G, K) 16 μL , and (D, H, L) 18 μL chloroform solution of oleylamine. (M, N) Plots of (M) the thickness and (N) the size as functions of volume of chloroform solution of oleylamine. Each dot is the average value of 20 sets of experimental data, and error bars show standard error.

current density–potential curves measured in an aqueous solution consisting of 0.5 M H_2SO_4 and 0.25 M HCOOH at a scan rate of 50 mV s^{-1} . The broad peaks at 0.23 V (versus Ag/AgCl) that appeared in both forward and reverse scan represented the direct oxidation of formic acid to CO_2 . According to the Nernst equation, the thermodynamic potential at this FA concentration was estimated to be -0.181 V (versus RHE). Thus, the overpotential for Pd nanosheets was calculated to be 0.288 V (versus RHE). The corresponding potentials versus RHE were shown by using top x -axis in Figure 4A. The catalytically inert performance of the substrate (Figure S6) also showed there was no contribution from the substrates. The presence of the oxidation peak in reverse scan was typically observed in Pd-catalyzed oxidation reactions (e.g., methanol, ethanol, glycerol, and formic acid) because only the reducing agents were accessible in the vicinity of Pd surface.²⁷ The equal height of the oxidation peaks in both the anodic and cathodic scan implied no loss of the active sites on catalyst surface during the forward and reverse oxidation.²⁸ It should be noted that the FA oxidation peaks in both forward and reverse scan are not necessary to occur at the same potential. The peak positions are related to various reaction conditions, such as scan rate (Figure S7), pH value, and the diffusion behavior of FA to Pd surface.^{29,30} The small shoulder at 0.5 V (versus Ag/AgCl) in forward scan could be attributed to the formation of oxide layer on Pd.³¹ The steep increase in the reverse scan indicated the efficient reduction of the Pd oxide layer built during the forward scan.²⁵ As compared, the curve of the commercial Pd black shared the similar shape in both forward and reverse scan, with a slightly higher

overpotential 0.308 V (versus RHE). However, the maximum mass current density of Pd nanosheets reached as high as 895.5 mA/mg at 0.23 V (versus Ag/AgCl), roughly 31 times larger than the commercial Pd black ($\sim 28.8 \text{ mA/mg}$ at 0.23 V versus Ag/AgCl). This value is also much higher than many Pd nanostructures reported in the literature, such as Pd nanoparticles (190 mA/mg),³² 3D Pd nanoflowers (211.3 mA/mg),³³ Pd tetrahedra (450 mA/mg),⁹ and Pd-based alloys (510 mA/mg)¹¹ and at the same level of other Pd nanoplates with a similar thickness but much smaller sizes.^{8,9,33}

The thickness-dependent catalytic activity was further investigated. Normalized by the nanosheet surface coverage, the current density slightly decreased as the nanosheet thickness increased (Figure S8), suggesting the thinner nanosheets have higher catalytic activity, probably due to the easier charge transport from catalyst to electrode. Among the four thicknesses, 2.3 nm thick nanosheets showed a slightly broader cathodic current than others, indicating higher catalytic activity. On the other hand, since smaller thickness corresponded to lower effective mass, the mass current density increased linearly from 701.7 to 1132.6 mA/mg when the thickness decreased from 3.2 to 2.0 nm (inset of Figure 4A and Figure S9). Despite the ultras-small thickness, the Pd nanosheets exhibited a superior stability compared to commercial Pd black. As shown in Figure 4B, after catalyzing FAO in the acid solution for 20 cycles, the maximum oxidation current of the Pd nanosheets decreased to 56% of the initial value, whereas the commercial Pd black only maintained 37% of the initial value. The higher stability of Pd nanosheets could be potentially attributed to the stronger adhesion to the substrates due to the

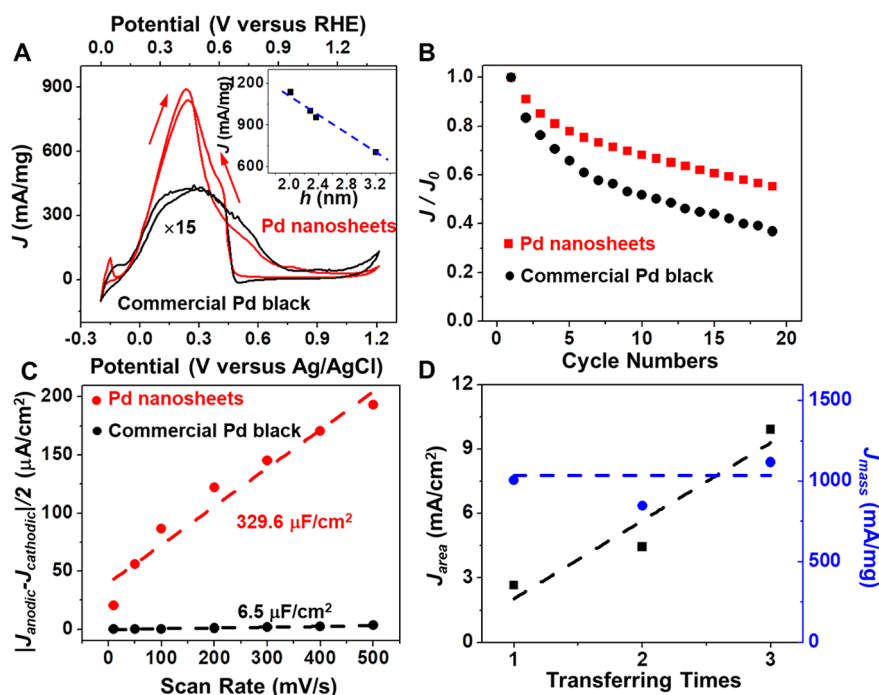


Figure 4. Electrocatalytic activities of palladium nanosheets for the oxidation of formic acid. (A) Current density (mass)–potential curves and (B) stabilities of palladium nanosheets and commercial palladium black as a comparison recorded in an aqueous solution containing 0.5 M H_2SO_4 and 0.25 M HCOOH at a scan rate of 50 mV s^{-1} . Inset shows the dependence of current density on the thickness of nanosheets. Straight blue dashed line serves as a guide to the eye. (C) Plot showing the extraction of the double-layer capacitance (C_{dl}) for palladium nanosheets and commercial palladium black. The dashed lines are linear fitting curves, with the slopes revealing C_{dl} . (D) Dependence of area current density (I_{area}) and mass current density (I_{mass}) on transferring times of palladium nanosheets from water–air interface to the substrates by scooping. Straight blue and black dashed lines serve as guides to the eye.

large and ultraflat contact area as compared to Pd black particles, which prohibited Pd nanosheets from dissolution or aggregation during the catalytic reactions.¹¹

The outstanding catalytic performance was attributed to the ultrahigh ratio of surface active sites to bulk volume arisen from the ultrathin feature. This merit was verified by measuring the double-layer capacitance (C_{dl}), which serves as an estimation of electrochemically active surface area.^{34,35} By normalizing the mass of Pd loading and plotting the anodic–cathodic current density difference versus scan rate using cyclic voltammetry measurements (Figure S10), C_{dl} was extracted from the slope according to the equation $C_{dl} = I/(dv/dt)$. As shown in Figure 4C, Pd nanosheets showed a C_{dl} of 329.6 $\mu\text{F}/\text{cm}^2$, 50.7 times higher than the commercial Pd black ($C_{dl} = 6.5 \mu\text{F}/\text{cm}^2$). This comparison confirmed that Pd nanosheets had a much higher specific electrochemically active surface area. In addition, given the monometallic and polycrystalline nature of the Pd nanosheets, the catalytic activity could be primarily attributed to the total exposed surface area rather than other geometric factors such as edges or side facets.

Considering the surface coverage of Pd nanosheets was much lower than 100%, the surface catalytic performance can be further improved by multiple-time transfer. More Pd nanosheets could be transferred to the support electrode surface after each additional transfer (Figure S11). Accordingly, the area current density increased linearly by 3.65 mA cm^{-1} per transfer (Figure 4D, black curve, the corresponding IV curves are shown in Figure S12). This incremental amount was nearly the same as the initial value, suggesting each transfer could introduce the same amount of catalytic active sites. Normalized by the mass of the nanosheets, the current density remained at

the same value of 1005.4 mA/mg (Figure 4D, blue curve). The constant mass current density suggested that all the nanosheets contributed the same to the catalytic reaction regardless of their sequence and location of being transferred.

CONCLUSION

In conclusion, ultrathin metallic Pd nanosheets with uniform thickness and quasi-square morphology were synthesized by ILE over a large area. These nanosheets were atomically flat with a surface roughness factor of $R_a = 0.184$. Electron microscopy revealed the Pd nanosheets were pure fcc phase polycrystalline with an average grain size of 12 nm. The size and thickness of the Pd nanosheets could be controlled by adjusting the packing density of the amphiphilic monolayer. As packing density increased, the thickness was tuned from 2.0 to 3.2 nm, and the average size increased from 1.83 to 5.24 μm . The extremely high surface-to-volume ratio arisen from the ultrathin feature together with the mixed exposure of crystal facets including highly active (100) facets yielded a significantly higher catalytic performance compared to Pd black. Particularly, the mass oxidation current reached as high as 1132.6 mA/mg when the nanosheet thickness was 2.0 nm. This value was the same as the highest reported value for Pd-based electrocatalyst and more than ~ 30 times higher than the commercial Pd black. This work presents an innovative solution of creating highly active electrocatalytic materials by controlled synthesis of a novel 2D morphology. The ultrahigh mass activity is particularly valuable for conserving the consumption of catalytic materials with high-cost and rare supplies.

EXPERIMENTAL SECTION

Synthesis of Pd Nanosheets. Pd nanosheets were synthesized by ILE. In a typical synthesis process, a 17 mL aqueous solution containing 0.25 mM tetrachloropalladic acid (H_2PdCl_4) was prepared in a glass vial. Then, 2 μL of formaldehyde (HCHO) was added into the precursor solution as a reducing agent. A 8 μL chloroform solution of oleylamine (~0.2 vol %) was dispersed on the surface of precursor solution, and the two-layer solution was exposed in atmosphere for 10 min to allow the chloroform to evaporate. Subsequently, the vial was sealed by a cap and placed in a 60 °C convection oven for 130 min for Pd nanosheets to grow. The vial was then taken out from the oven. The Pd nanosheets were then immediately transferred onto a Si substrate by scooping at the surface of the reaction solution, i.e., simply dipping the substrate into the solution and then lifting.

Characterization. A Zeiss LEO 1530 field-emission scanning electron microscope was used to study the morphologies of the nanosheets. Atomic force microscopy (AFM) tomography images were obtained using an XE-70 Park System. X-ray photoelectron spectroscopy (XPS) spectrum was obtained from a Thermo Scientific K-alpha XPS instrument with a 100 μm spot size, with the flood gun turned on during the measurements. FEI TF30 transmission electron microscope operated at 300 kV was used to study the crystal structure. Energy-dispersive X-ray spectrum (EDX) and EDX mapping were taken using the STEM mode on a probe aberration corrected FEI Titan operated at 200 kV.

Electrochemical Measurements. The electrochemical measurements were carried out on an autolab PGSTAT302N station, using a typical three-electrode setup, with Pd nanosheets/commercial Pd black as the working electrode, a Pt wire as the counter electrode, and Ag/AgCl as the reference electrode. The working electrodes were prepared by transferring Pd nanosheets and commercial Pd black onto Si substrates coated with 100 nm thick Au thin film. For Pd nanosheets, the transferring was simply achieved by collecting the nanosheets onto substrates by the same approach described above. Pd nanosheets were then annealed in Ar atmosphere at 200 °C for 2 h to remove oleylamine surfactants from the surface. For commercial Pd black, a typical loading process was employed. 15 μL of ink of commercial Pd black dispersion containing 850 μL of isopropanol, 150 μL of DI water, and 50 μL of Nafion was dropped onto the substrates. Then, the substrates with Pd black dispersion were placed in a 90 °C oven for 10 min to dry. Electrocatalytic activity was evaluated in a solution containing 0.5 M H_2SO_4 and 0.25 M formic acid, when scanning the voltage from -0.2 to 1.2 V with the scan rate of 50 mV/s. Electrochemically active surface area was characterized in the solution of 0.5 M H_2SO_4 , with a series of scan rate of 10, 50, 100, 200, 300, 400, and 500 mV/s to scan the voltage from 0.2 to 0.3 V in order to extract the double-layer capacitance (C_{dl}).

ASSOCIATED CONTENT

Supporting Information

The Supporting Information is available free of charge on the ACS Publications website at DOI: 10.1021/acs.chemmater.8b00575.

SEM images of Pd nanosheets with spikes at the corners and with a terraced morphology, a full wavelength survey scan of XPS spectrum, low magnification TEM image of one Pd nanosheet, SEM image of commercial Pd black, J - V curves of thickness dependent activity, cyclic voltammetry curves, SEM images of Pd nanosheets after multiple-time transfer, J - V curves of the catalytic activity after multiple transfer (PDF)

AUTHOR INFORMATION

Corresponding Author

*E-mail: xudong.wang@wisc.edu (X.W.).

ORCID

Xin Yin: 0000-0002-4759-0226

Paul M. Voyles: 0000-0001-9438-4284

Xudong Wang: 0000-0002-9762-6792

Notes

The authors declare no competing financial interest.

ACKNOWLEDGMENTS

This work is supported by Army Research Office (ARO) under Grant W911NF-16-1-0198 and National Science Foundation through the University of Wisconsin Materials Research Science and Engineering Center (DMR-1121288).

REFERENCES

- (1) Cargnello, M.; Doan-Nguyen, V. V.; Gordon, T. R.; Diaz, R. E.; Stach, E. A.; Gorte, R. J.; Fornasiero, P.; Murray, C. B. Control of metal nanocrystal size reveals metal-support interface role for ceria catalysts. *Science* **2013**, *341*, 771–773.
- (2) Habas, S. E.; Lee, H.; Radmilovic, V.; Somorjai, G. A.; Yang, P. Shaping binary metal nanocrystals through epitaxial seeded growth. *Nat. Mater.* **2007**, *6*, 692–697.
- (3) Larsson, E. M.; Langhammer, C.; Zorić, I.; Kasemo, B. Nanoplasmonic probes of catalytic reactions. *Science* **2009**, *326*, 1091–1094.
- (4) Linic, S.; Christopher, P.; Ingram, D. B. Plasmonic-metal nanostructures for efficient conversion of solar to chemical energy. *Nat. Mater.* **2011**, *10*, 911–921.
- (5) Seo, W. S.; Lee, J. H.; Sun, X.; Suzuki, Y.; Mann, D.; Liu, Z.; Terashima, M.; Yang, P. C.; McConnell, M. V.; Nishimura, D. G.; Dai, H. FeCo/graphitic-shell nanocrystals as advanced magnetic-resonance-imaging and near-infrared agents. *Nat. Mater.* **2006**, *5*, 971–976.
- (6) Sun, S.; Murray, C. B.; Weller, D.; Folks, L.; Moser, A. Monodisperse FePt nanoparticles and ferromagnetic FePt nanocrystal superlattices. *Science* **2000**, *287*, 1989–1992.
- (7) Xia, Y.; Xiong, Y.; Lim, B.; Skrabalak, S. E. Shape-controlled synthesis of metal nanocrystals: Simple chemistry meets complex physics? *Angew. Chem., Int. Ed.* **2009**, *48*, 60–103.
- (8) Huang, X.; Tang, S.; Mu, X.; Dai, Y.; Chen, G.; Zhou, Z.; Ruan, F.; Yang, Z.; Zheng, N. Freestanding palladium nanosheets with plasmonic and catalytic properties. *Nat. Nanotechnol.* **2011**, *6*, 28–32.
- (9) Zhang, Y.; Wang, M.; Zhu, E.; Zheng, Y.; Huang, Y.; Huang, X. Seedless Growth of Palladium Nanocrystals with Tunable Structures: From Tetrahedra to Nanosheets. *Nano Lett.* **2015**, *15*, 7519–7525.
- (10) Jin, M.; Zhang, H.; Xie, Z.; Xia, Y. Palladium nanocrystals enclosed by {100} and {111} facets in controlled proportions and their catalytic activities for formic acid oxidation. *Energy Environ. Sci.* **2012**, *5*, 6352–6357.
- (11) Guo, S.; Zhang, S.; Sun, X.; Sun, S. Synthesis of ultrathin FePtPd nanowires and their use as catalysts for methanol oxidation reaction. *J. Am. Chem. Soc.* **2011**, *133*, 15354–15357.
- (12) Li, L.; Zhao, S.; Joshi-Pangu, A.; Diane, M.; Biscoe, M. R. Stereospecific Pd-catalyzed cross-coupling reactions of secondary alkylboron nucleophiles and aryl chlorides. *J. Am. Chem. Soc.* **2014**, *136*, 14027–14030.
- (13) Stille, J. K. The palladium-catalyzed cross-coupling reactions of organotin reagents with organic electrophiles [new synthetic methods (58)]. *Angew. Chem., Int. Ed. Engl.* **1986**, *25*, 508–524.
- (14) Nicolaou, K.; Bulger, P. G.; Sarlah, D. Palladium-catalyzed cross-coupling reactions in total synthesis. *Angew. Chem., Int. Ed.* **2005**, *44*, 4442–4489.
- (15) Zeng, X.; Latimer, M.; Xiao, Z.; Panuganti, S.; Welp, U.; Kwok, W.; Xu, T. Hydrogen gas sensing with networks of ultrasmall palladium nanowires formed on filtration membranes. *Nano Lett.* **2011**, *11*, 262–268.
- (16) Favier, F.; Walter, E. C.; Zach, M. P.; Benter, T.; Penner, R. M. Hydrogen sensors and switches from electrodeposited palladium mesowire arrays. *Science* **2001**, *293*, 2227–2231.

(17) Tittl, A.; Mai, P.; Taubert, R.; Dregely, D.; Liu, N.; Giessen, H. Palladium-based plasmonic perfect absorber in the visible wavelength range and its application to hydrogen sensing. *Nano Lett.* **2011**, *11*, 4366–4369.

(18) Li, Y.; Yan, Y.; Li, Y.; Zhang, H.; Li, D.; Yang, D. Size-controlled synthesis of Pd nanosheets for tunable plasmonic properties. *CrystEngComm* **2015**, *17*, 1833–1838.

(19) Zhang, Z.; Liu, Y.; Chen, B.; Gong, Y.; Gu, L.; Fan, Z.; Yang, N.; Lai, Z.; Chen, Y.; Wang, J. Submonolayered Ru deposited on ultrathin Pd nanosheets used for enhanced catalytic applications. *Adv. Mater.* **2016**, *28*, 10282–10286.

(20) Wang, F.; Seo, J.-H.; Luo, G.; Starr, M. B.; Li, Z.; Geng, D.; Yin, X.; Wang, S.; Fraser, D. G.; Morgan, D.; Ma, Z.; Wang, X. Nanometre-thick single-crystalline nanosheets grown at the water–air interface. *Nat. Commun.* **2016**, *7*, 10444.

(21) Wang, F.; Yin, X.; Wang, X. Morphological control in the adaptive ionic layer epitaxy of ZnO nanosheets. *Extreme Mech. Lett.* **2016**, *7*, 64–70.

(22) Yin, X.; Shi, Y.; Wei, Y.; Joo, Y.; Gopalan, P.; Szlufarska, I.; Wang, X. Unit Cell Level Thickness Control of Single-Crystalline Zinc Oxide Nanosheets Enabled by Electrical Double-Layer Confinement. *Langmuir* **2017**, *33*, 7708–7714.

(23) Siril, P. F.; Ramos, L.; Beaunier, P.; Archirel, P.; Etcheberry, A.; Remita, H. Synthesis of ultrathin hexagonal palladium nanosheets. *Chem. Mater.* **2009**, *21*, 5170–5175.

(24) Long, R.; Mao, K.; Ye, X.; Yan, W.; Huang, Y.; Wang, J.; Fu, Y.; Wang, X.; Wu, X.; Xie, Y.; Xiong, Y. Surface facet of palladium nanocrystals: A key parameter to the activation of molecular oxygen for organic catalysis and cancer treatment. *J. Am. Chem. Soc.* **2013**, *135*, 3200–3207.

(25) Mazumder, V.; Sun, S. Oleylamine-mediated synthesis of Pd nanoparticles for catalytic formic acid oxidation. *J. Am. Chem. Soc.* **2009**, *131*, 4588–4589.

(26) Lee, H.; Habas, S. E.; Somorjai, G. A.; Yang, P. Localized Pd overgrowth on cubic Pt nanocrystals for enhanced electrocatalytic oxidation of formic acid. *J. Am. Chem. Soc.* **2008**, *130*, 5406–5407.

(27) Bianchini, C.; Shen, P. K. Palladium-based electrocatalysts for alcohol oxidation in half cells and in direct alcohol fuel cells. *Chem. Rev.* **2009**, *109*, 4183–4206.

(28) Capon, A.; Parsons, R. The oxidation of formic acid on noble metal electrodes: II. A comparison of the behaviour of pure electrodes. *J. Electroanal. Chem. Interfacial Electrochem.* **1973**, *44*, 239–254.

(29) Brimaud, S.; Solla-Gullón, J.; Weber, I.; Feliu, J. M.; Behm, R. J. Formic Acid Electrooxidation on Noble-Metal Electrodes: Role and Mechanistic Implications of pH, Surface Structure, and Anion Adsorption. *ChemElectroChem.* **2014**, *1*, 1075–1083.

(30) Elgrishi, N. m.; Rountree, K. J.; McCarthy, B. D.; Rountree, E. S.; Eisenhart, T. T.; Dempsey, J. L. A Practical Beginner's Guide to Cyclic Voltammetry. *J. Chem. Educ.* **2018**, *95*, 197–206.

(31) Ali, H.; Kanodarwala, F. K.; Majeed, I.; Stride, J. A.; Nadeem, M. A. La₂O₃ Promoted Pd/rGO electro-catalysts for formic acid oxidation. *ACS Appl. Mater. Interfaces* **2016**, *8*, 32581–32590.

(32) Mazumder, V.; Chi, M.; Mankin, M. N.; Liu, Y.; Metin, O. n.; Sun, D.; More, K. L.; Sun, S. A facile synthesis of MPd (M= Co, Cu) nanoparticles and their catalysis for formic acid oxidation. *Nano Lett.* **2012**, *12*, 1102–1106.

(33) Qiu, X.; Zhang, H.; Wu, P.; Zhang, F.; Wei, S.; Sun, D.; Xu, L.; Tang, Y. One-Pot Synthesis of Freestanding Porous Palladium Nanosheets as Highly Efficient Electrocatalysts for Formic Acid Oxidation. *Adv. Funct. Mater.* **2017**, *27*, 1603852.

(34) Yu, Y.; Zhang, Z.; Yin, X.; Kvit, A.; Liao, Q.; Kang, Z.; Yan, X.; Zhang, Y.; Wang, X. Enhanced photoelectrochemical efficiency and stability using a conformal TiO₂ film on a black silicon photoanode. *Nat. Energy* **2017**, *2*, 17045.

(35) Cabán-Acevedo, M.; Stone, M. L.; Schmidt, J.; Thomas, J. G.; Ding, Q.; Chang, H.-C.; Tsai, M.-L.; He, J.-H.; Jin, S. Efficient hydrogen evolution catalysis using ternary pyrite-type cobalt phosphosulphide. *Nat. Mater.* **2015**, *14*, 1245–1251.